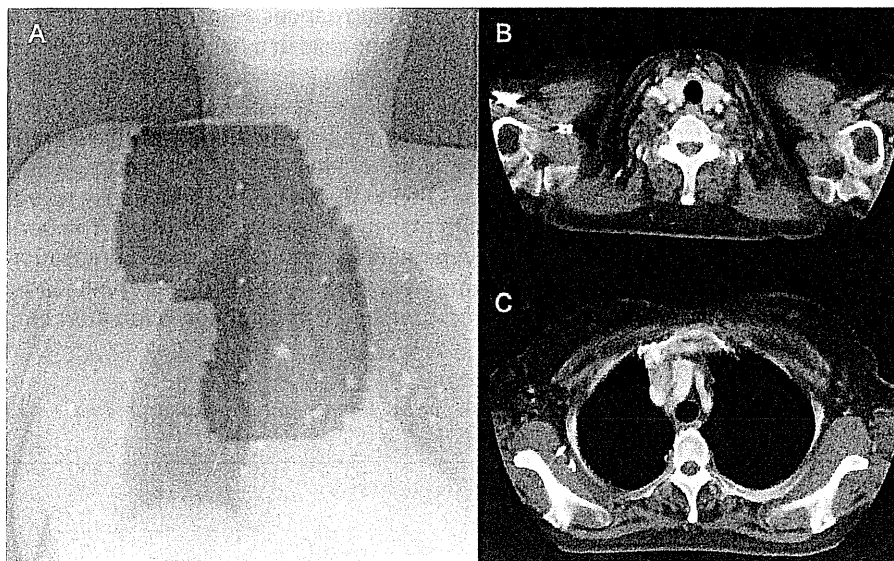**Figure 1.** (A and B) Computed tomography (CT) image showing a mass lesion in the right chest wall and a peripheral lung nodule. (C and D) [18 F] fluorodeoxy-glucose (FDG) positron emission tomography-CT showing elevated FDG uptake reflective of disease activity.


Figure 2. (A) Pre-defined radiation field. (B and C) CT image showing supraclavicular and mediastinal lymphadenopathy.

clinical trial to support adjuvant chemotherapy or radiotherapy. One year after the surgery, a routine follow-up CT had revealed post-surgical recurrences in the mediastinal and right supraclavicular lymph nodes, and the patient had received cisplatin and vinorelbine with concurrent thoracic radiotherapy (60 Gray in 30 fractions) (Fig. 2). Thereafter, the patient was followed up regularly with whole body CT every 6 months and additional brain magnetic resonance imaging properly.

There was no evidence of recurrence until 7 years after the initiation of chemoradiotherapy.

Histopathological examination of a biopsy specimen from the tumor in the right upper chest revealed proliferation of spindle-shaped malignant tumor cells in a background of osteoid, consistent with osteosarcoma (Fig. 3). The location of the main lesion corresponded to the radiation field used for the chemoradiotherapy. Based on the clinical information and
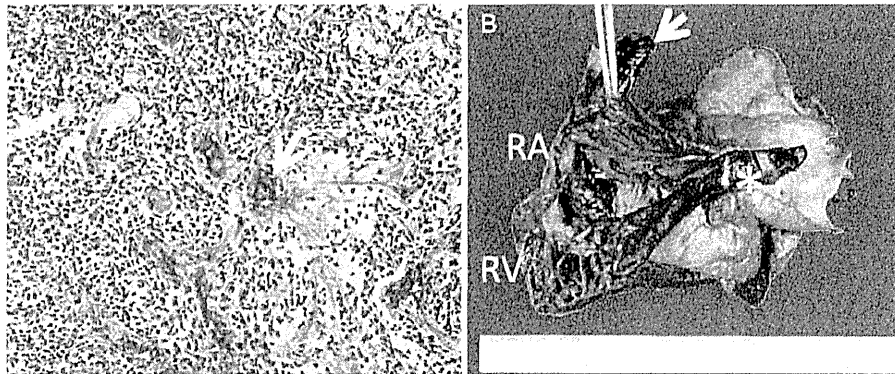
Figure 3. (A) Proliferation of spindle-shaped malignant tumor cells in a background of osteoid (white arrow), consistent with the diagnosis of osteosarcoma. (B) Contiguous invasion of the superior vena cava (white arrow), right atrium, right ventricle and pulmonary artery (asterisk) by the osteosarcoma.

histopahological findings, the patient was diagnosed as having secondary osteosarcoma developing as a result of the chemoradiotherapy administered previously for the recurrent NSCLC. Unfortunately, the patient died of respiratory failure as a result of rapid progression of the osteosarcoma within a week of hospitalization.

In the macroscopic examination at autopsy, the tumor showed contiguous invasion of the superior vena cava, right atrium, right ventricle and pulmonary arteries, with massive thrombus formation (Fig. 3). The peripheral pulmonary arteries were diffusely occluded with metastatic tumors, with multiple pulmonary infarctions in the left lower lobe of the lung. Neither macroscopic nor microscopic examinations revealed any evidence of recurrence of the NSCLC.

DISCUSSION

We report a case of extraordinarily rapidly progressive osteosarcoma developing 10 years after curative chemoradiotherapy for NSCLC. Osteosarcomas are the most frequently encountered bone tumors in clinical practice and are almost always highly malignant. Post-radiation osteosarcomas account for 3.4–5.5% of all osteosarcomas and 50–60% of all radiation-induced sarcomas (RISs) (1).

RIS is an uncommon long-term complication of radiotherapy, occurring with an incidence rate ranging from 0.03 to 0.80%. The most commonly reported primary cancers in such patients are breast cancer (30%), uterine cancer (28%) and lung cancer (5%), and, in a report from Finland, the reported incidence ratio of secondary sarcoma after adjustment for sex and age was 3.4 in patients treated by chemoradiotherapy, 3.2 by radiotherapy and 4.9 by chemotherapy (2). There are two detailed reports of secondary malignancy after chemoradiotherapy for locally advanced NSCLC (3,4). In these reports, a total of 16 secondary malignancies out of 154 patients were found and the relative risk rate of any secondary malignancy was reported as 2.4–2.8%. Of the 16 patients with secondary malignancy, the types of malignancy were as follows: five with lung cancer, three with esophagus cancer, two with stomach cancer and none with sarcoma, respectively.

With regard to the biological behavior for these tumors, RIS is thought to be more aggressive than spontaneously occurring tumor. In a relatively large retrospective study of RIS, the 5-year survival rate was 39% in patients treated by surgery and 0% in those treated by chemotherapy, suggesting the aggressive biological behavior of these tumors (5). Although the precise mechanism of its aggressiveness is unknown, it could be assumed that some genetic instabilities, such as c-myc amplification of radiation-induced angiosarcoma, contributed to the more aggressive feature of RIS occurrence than spontaneous sarcoma (6). Similarly, in our patient also, the tumor showed more rapid progression than what would be expected in a case of a spontaneous sarcoma.

The standard of care for locally advanced NSCLC changed from radiotherapy to chemoradiotherapy in the 1990s, and many patients survive long enough to be at risk for the development of secondary malignancies related to definitive chemoradiotherapy. Our case serves to highlight the risk of development of secondary sarcoma as a life-threatening late complication after chemoradiotherapy, even after a complete cure of the primary tumor.

Funding

None declared.

Conflict of interest statement

None declared.

References

1. Christopher DM, Fletcher KKU, Mertens F. *Pathology and Genetics of Tumours of Soft Tissue and Bone.* World Health Organization Classification of Tumours. Lyon: IARC Press, 2002. 264–285.
2. Virtanen A, Pukkala E, Auvinen A. Incidence of bone and soft tissue sarcoma after radiotherapy: a cohort study of 295, 712 Finnish cancer patients. *Int J Cancer* 2006;118:1017–21.
3. Kawaguchi T, Matsumura A, Iuchi K, et al. Second primary cancers in patients with stage III non-small cell lung cancer successfully treated with chemo-radiotherapy. *Jpn J Clin Oncol* 2006;36:7–11.

4. Takigawa N, Kiura K, Segawa Y, et al. Okayama Lung Cancer Study G. Second primary cancer in survivors following concurrent chemoradiation for locally advanced non-small-cell lung cancer. *Br J Cancer* 2006;95:1142–4.

5. Jean-Leon Lagrange M, PhD, Alain Ramaioli P, Marie-Christine Chateau M, Christian Marchal M. Sarcoma after radiation therapy: retrospective multiinstitutional study of 80 histologically confirmed cases. *Radiology* 2000;216:197–205.

6. Manner J, Radlwimmer B, Hohenberger P, et al. MYC high level gene amplification is a distinctive feature of angiosarcomas after irradiation or chronic lymphedema. *Am J Pathol* 2010;176:34–9.

Original Article

Histopathological characteristics of hypervascular cholangiocellular carcinoma as an early stage of cholangiocellular carcinoma

Yuya Sato,[1,4] Hidenori Ojima,[1] Hiroaki Onaya,[2] Taisuke Mori,[1] Nobuyoshi Hiraoka,[1] Yoji Kishi,[3] Satoshi Nara,[3] Minoru Esaki,[3] Kazuaki Shimada,[3] Tomoo Kosuge,[3] Kenich Sugihara[4] and Yae Kanai[1]

[1]*Division of Molecular Pathology, National Cancer Center Research Institute,* [2]*Diagnostic Radiology Division,* [3]*Hepatobiliary and Pancreatic Surgery Division, National Cancer Center Hospital, and* [4]*Department of Surgical Oncology, Graduate School, Tokyo Medical and Dental University, Tokyo, Japan*

Aim: Prognosis of hypervascular cholangiocellular carcinoma (h-CCC) is reportedly better than that of ordinary hypovascular CCC (o-CCC). The aim of this study is to clarify the histopathological characteristics of h-CCC.

Methods: On the basis of the findings in the arterial phase of contrast-enhanced computed tomography, 16 cases of mass-forming-type CCC were divided into two groups (h-CCC, *n* = 8; o-CCC, *n* = 8). Areas of high (Area H-a) and low (Area H-b) attenuation in h-CCC cases and areas of low attenuation in o-CCC cases (Area O) were delineated. These areas were then evaluated histopathologically to determine the proportion of tumor cells, fibrous stroma, arterial vessel density, and immunohistochemical expression of Vascular endothelial growth factor; angiopoietin-2; cytokeratin 7, CK19, *SOX9* and *SOX17* genes; epithelial cell adhesion molecule; and the Bmi-1, Ki-67, epithelial membrane antigen and polyclonal carcinoembryonic antigen.

Results: The areal ratio of tumor cells decreased and that of fibrous stroma increased in the following order: Area H-a,

Area H-b and Area O. Values for AVD and neural cell adhesion molecule positivity rate were significantly higher in Area H-a than in Areas H-b or O. Expressions of vascular endothelial growth factor and angiopoietin-2 were significantly higher in Areas H-a and H-b than in Area O. The Ki-67 labeling index increased in the following order: Area H-a, Area H-b and Area O.

Conclusion: A high areal ratio of tumor cells and AVD as well as a high expression of stem cells and angiogenic markers were observed in cases of h-CCC, whereas the areal ratio of fibrous stroma and malignant potential were low. These results suggest that h-CCC may represent the early stage of CCC.

Key words: angiogenesis, arterial vessel density, cholangiocellular carcinoma, dynamic computed tomography, immunohistochemistry, stem cell marker

INTRODUCTION

CHOLANGIOCELLULAR CARCINOMA (CCC) is the second most common primary liver cancer and a highly malignant invasive carcinoma arising through malignant transformation of cholangiocytes.[1] In the arterial phase of contrast-enhanced computed tomogra-

phy (CT) with delayed peripheral enhancement in the equilibrium phase, CCC is generally visualized as a hypovascular tumor of low attenuation relative to the surrounding liver parenchyma.[2,3] However, in some cases, CT reveals CCC to be hypervascular and highly attenuated in the arterial phase.[4,5] The proportion of hypervascular CCC (h-CCC) diagnosed on the basis of diagnostic imaging has varied from 5% to 47% in previous reports.[2,3,6–9] Survival in patients with h-CCC is reportedly better than that in patients with hypovascular CCC.[2,10] Some cases of h-CCC have been identified as cholangiocellular carcinoma (CoCC),[10,11] which is classified as a stem cell variant of combined

hepatocellular–cholangiocarcinoma.[12] However, the clinicopathological characteristics of h-CCC have yet to be fully clarified.

To describe these characteristics, a clear and reproducible radiological definition of h-CCC must be established. In addition, a detailed pathological/radiological correlation must be outlined. However, only a few applicable cases are available for this purpose. The aim of this study was to clarify the histopathological and immunohistochemical (IHC) characteristics of h-CCC and determine the clinicopathological differences between it and hypovascular CCC on the basis of an objective radiological definition.

METHODS

Patients and specimen selection

BETWEEN OCTOBER 2002 and April 2010, adenocarcinoma was diagnosed histologically, and surgery for CCC was performed in 107 patients at the National Cancer Center Hospital, Tokyo, Japan. Of these, mass-forming-type CCC was macroscopically identified in 47 patients on the basis of the World Health Organization Classification of Tumors of the Digestive System, 4th edition.[12] This type of CCC was deemed suitable for determination of a correlation between the radiological and pathological characteristics of CCC. One radiologist and one pathologist compared the preoperative CT findings and the macroscopic features of each resected specimen in all 47 cases. Among the 47 cases, 16 showed complete correlation between CT findings and pathological findings. All 16 patients underwent curative surgery. Detailed clinical data are described in Table S1. The largest available transverse sections were selected for this study. This study was approved by the ethics committee of the National Cancer Center, Tokyo, Japan.

CT protocol

All scans were obtained by the means of multidetector row helical CT units (Aquilion; Toshiba Medical Systems, Tokyo, Japan) that had 16 or 64 detector rows, a 0.5-s rotation time, and exposure factors of 120 kV and 50–500 mAs using automatic exposure control for all scans. The contrast material injection rate was set at 2.7–3.3 mL/s, and the contrast material was injected into the antecubital vein with an automatic power injector (DUAL SHOT GX; Nemoto, Tokyo, Japan) via a 20-G i.v. catheter. Before contrast material injection, an unenhanced scan was performed in the transverse plane.

Contrast-enhanced CT was obtained after i.v. injection of iopamidol (Iopamiron 300/370; Bayer Schering Pharma, Osaka, Japan). The arterial phase was started 40 s after the onset of injection, the portal phase at 70 s and the equilibrium phase at 180 s. Images with an effective 1-mm section thickness were reconstructed every 1 mm to provide contiguous sections.

Image assessment

Images of the largest transverse sections of the tumors were evaluated by a radiologist (H. O.). All interpretations were made from axial CT images on a monitor, and the observer was blinded to the pathological and clinical findings. Lesions with a heterogeneous enhancement pattern on contrast-enhanced images were categorized according to the predominating attenuation (>50%) in the lesion, as described previously.[5,13] Tumors were then classified into two groups according to their enhancement patterns in the arterial phase of CT. If a high-attenuation area (compared with the background liver parenchyma) accounted for more than 50% of the largest slice, the tumor was classified as h-CCC, whereas high-attenuation accounting for less than 50% was classified as hypovascular CCC (ordinary hypovascular CCC; o-CCC). Distribution percentages of hypervascular area in eight h-CCC and in eight o-CCC cases are described in Figure 1.

Table 1 summarizes the clinicopathological data and attenuation patterns for patients with h-CCC and o-CCC. Attenuation patterns were classified into the following four types according to Kim *et al.*'s report:[5] homogeneous enhancement, heterogeneous enhancement, peripheral enhancement, and a mix of rim and internal enhancement. Attenuation values within the tumors were measured objectively in Hounsfield units (HU) using a circular region of interest (ROI). The ROI cursor was located in a relatively homogeneous area in the heterogeneously enhanced tumor (Fig. 2). Five ROI cursors were also placed in the background liver parenchyma adjacent to the tumor in the same slice for measurement of mean attenuation values. Correlation analysis was then performed between the attenuation values of ROI in the tumors and the mean attenuation values of the background liver parenchyma. Detailed data of attenuation values in each area is described in Table S2. A difference of more than 20 HU between attenuation values was considered significant.

In h-CCC tumors, any area of high attenuation (with an attenuation value exceeding that of the background liver parenchyma) in the arterial phase of CT was designated an Area H-a component, and any area of low
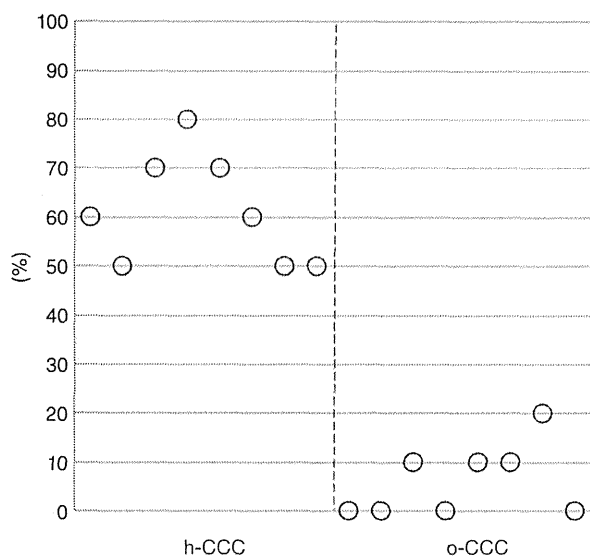
Figure 1 Distribution percentage of hypervascular area in eight hypervascular cholangiocellular carcinoma (h-CCC) and in eight ordinary hypovascular CCC (o-CCC). If high-attenuation areas (compared with the background liver parenchyma) accounted for more than 50% of the largest slice, the tumor was classified as h-CCC, whereas if high-attenuation areas accounted for less than 50%, the tumor was classified as o-CCC.

attenuation (with an attenuation value lower than that of the background liver parenchyma) was designated an Area H-b component. Areas of low attenuation in o-CCC (Area O) were also delineated. The histopathological features in each area (Area H-a, Area H-b and Area O) were then examined.

Histopathological evaluation

For all 16 tumors, two pathologists (Y. S. and H. O.) examined the histopathological features in each area (Area H-a, Area H-b and Area O) without knowledge of the clinical data (Fig. 3). After standard histopathological examination, the proportion of tumor cells and fibrous stroma in each area was determined, and various types of immunostaining were performed.

Evaluation of the areal ratio of tumor cells and fibrous stroma

Areas of fibrous stroma and vacant spaces were visualized in histopathological images stained with hematoxylin–eosin (HE, original magnification ×100) using Photoshop Elements version 7.0 (Adobe, San Jose,

CA, USA). Areas containing tumor cells, fibrous stroma and vacant spaces in five fields were measured using Image J software version 1.46c (National Institutes of Health freeware). After subtracting the area of vacant spaces, the areal ratio of tumor cells and fibrous stroma were calculated. Inflammatory cells and stromal cells were regarded as fibrous stroma.

IHC staining

Immunohistochemistry for h-caldesmon and the neural cell adhesion molecule (NCAM) was performed using an Autostainer (Dako, Glostrup, Denmark). Vascular endothelial growth factor (VEGF); angiopoietin-2 (Ang-2); cytokeratin 7 (CK7), CK19, SOX9, SOX17, epithelial cell adhesion molecule (EpCAM); and the Bmi-1, Ki-67, epithelial membrane antigen (EMA) and polyclonal carcinoembryonic antigen (pCEA) markers were immunostained using the avidin–biotinylated peroxidase complex method (Envision Dual Link System-HRP; Dako). Sources and dilutions of the primary antibodies are listed in Table S3.

Formalin-fixed, paraffin-embedded serial tissue sections (4 μm) were placed on silane-coated slides for IHC

Table 1 Summary of clinicopathological data for patients with h-CCC and o-CCC

	h-CCC ($n = 8$)	o-CCC ($n = 8$)
Sex		
Male	4	7
Female	4	1
Age (years)†	60.8 ± 8.8	60.6 ± 11.9
Chronic viral hepatitis (HBV)	3	0
Chronic viral hepatitis (HCV)	0	1
Tumor size (mm)†	60.3 ± 19.2	73.4 ± 43.2
Pathology		
Well	2	1
Moderate	6	6
Poor	0	1
Attenuation pattern		
Homogeneous enhancement	0	—
Heterogeneous enhancement	2	—
Peripheral enhancement	0	—
Mix of rim and internal heterogeneous enhancement	6	—
5-year survival	87.5%	62.5%

†Average ± standard deviation.
HBV, hepatitis B virus; HCV, hepatitis C virus; h-CCC, hypervascular cholangiocellular carcinoma; o-CCC, ordinary hypovascular CCC.
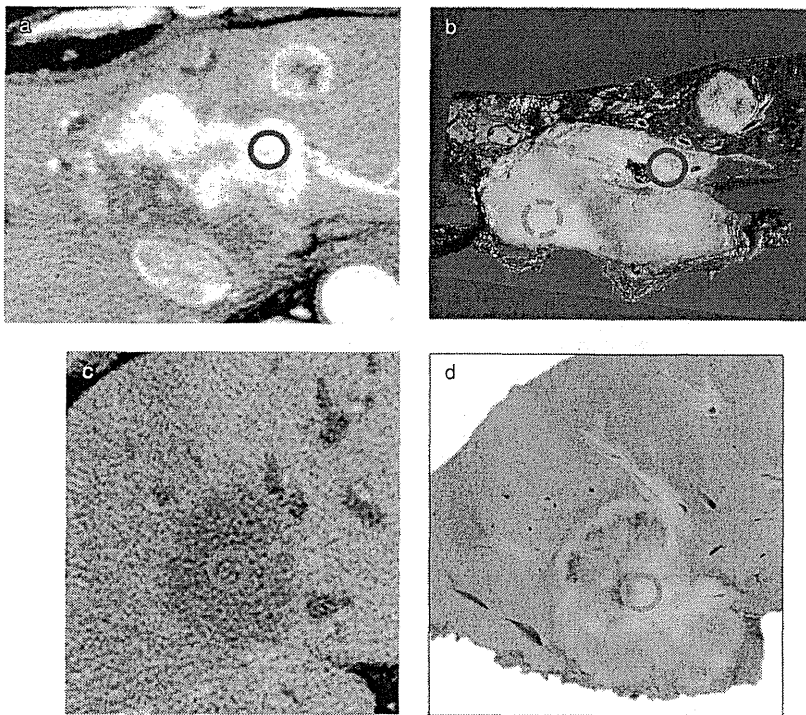
Figure 2 Representative images of tumors in the early phase of dynamic computed tomography (CT) and corresponding macroscopic images. Hypervascular CCC (h-CCC) (a). Ordinary hypovascular CCC (o-CCC) (c). The high-attenuation area in h-CCC was labeled as the Area H-a component (surrounded by the solid line), the low-attenuation area in h-CCC was labeled as the Area H-b component (surrounded by the dotted line), and the low-attenuation area in o-CCC (representative area in o-CCC) was labeled as the Area O component (surrounded by the solid line). Pathological features of Area H-a, Area H-b (b), and Area O (d) were examined.

analysis. The sections were deparaffinized and rehydrated in xylene and grade-diluted ethanol (50–100%), then immersed for 20 min in 0.3% hydrogen peroxide with absolute methanol to block endogenous peroxidase activity. For CK7, CK19, Ki-67, EMA and pCEA, antigen retrieval was performed by heating in 0.01 M citrate buffer (pH 6.0) at 121°C for 10 min in an autoclave. For VEGF, Ang-2, SOX9, SOX17, EpCAM and Bmi-1, antigen retrieval was performed by heating Tris-ethylenediaminetetraacetic acid buffer (pH 9.0) at 98°C for 40 min in a water bath. After protein blocking, the sections were incubated with each primary antibody at room temperature overnight, and then incubated with Envision Dual Link reagent (Dako) at room temperature for 30 min and visualized using 3,3′-diaminobenzidine tetrahydrochloride as a chromogen. Finally, the sections were counterstained with hematoxylin and gently rinsed in phosphate-buffered saline between incubation steps.

IHC evaluation

All IHC findings were evaluated and interpreted without the knowledge of the clinicopathological data by three pathologists (Y. S., H. O. and T. M.).

Arterial vessel density (AVD) was calculated by counting h-caldesmon positive arteries in five representative high-power (×200) fields (×20 objective lens and ×10 ocular lens; 0.7386 mm^2 per field) in each area.[14] Portal or central veins with a smooth muscle layer, h-caldesmon positive large arteries and brown-stained single cells were not counted. The average count of h-caldesmon positive arteries in the five fields was recorded as the AVD in each area. IHC expression of VEGF and Ang-2 was defined as follows:[15] 0+, no cytoplasmic staining; 1+, faint cytoplasmic staining (equivalent to the intensity of vascular epithelium of the normal liver for Ang-2); and 2+, strong cytoplasmic staining (equivalent to the intensity of normal hepatocytes for VEGF). The final score was considered positive if more than 50% of the tumor cells (200 cells selected randomly in each area) were scored as 2+. Expressions of CK7 and CK19 were considered positive if more than 5% of the tumor cells were stained. SOX9, SOX17 and EpCAM immunostaining was defined as follows: 0+, less than 1% of tumor cells stained; 1+, faint cytoplasmic staining in more than 1% of the tumor cells; 2+, moderate cytoplasmic staining in more than 1% of the tumor cells; and 3+, strong cytoplasmic staining in more than 1% of the tumor cells. Finally, a score of 2+ or 3+ was defined as positive, and a score of 0+ or 1+ was defined as negative. NCAM expression was defined as

(A)

(B)
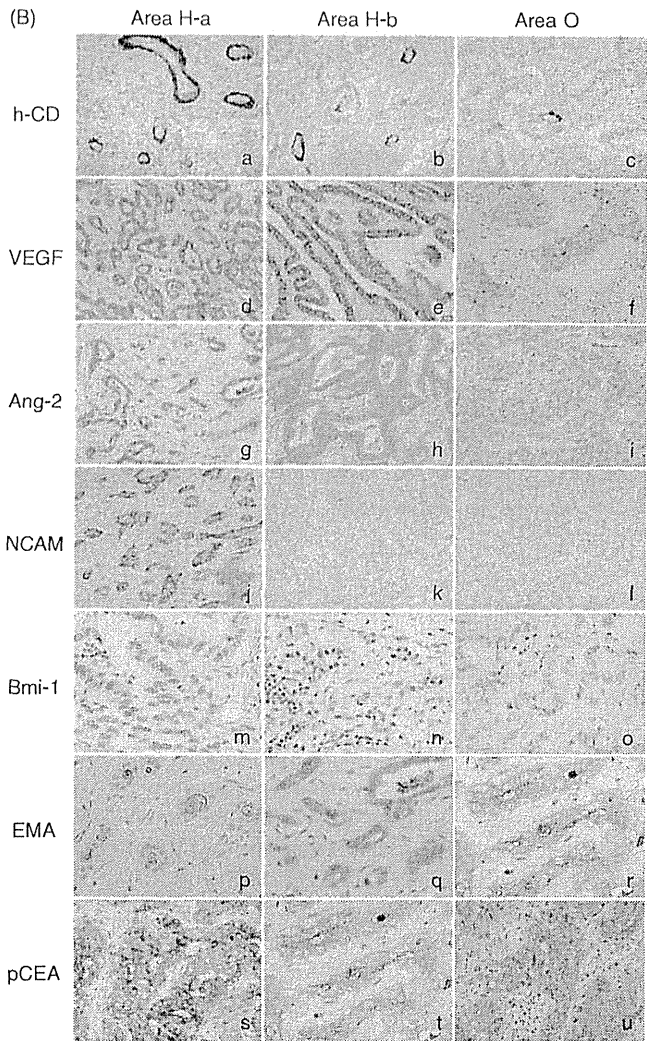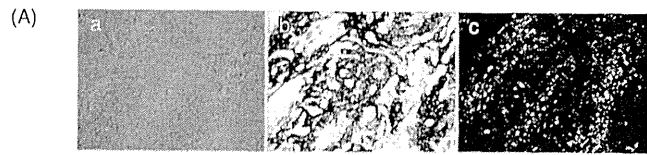
Figure 3 (A) The areal ratio of tumor cells and fibrous stroma. Areas of fibrous stroma (b) and vacant spaces (c) were visualized in histopathological images (hematoxylin–eosin, original magnification ×100) (a). (B) Representative images of immunohistochemical staining (h-caldesmon [h-CD] [a–c], vascular endothelial growth factor [VEGF] [d–f], angiopoietin-2 [Ang-2] [g–i], neural cell adhesion molecule [NCAM] [j–l], Bmi-1 [m–o], epithelial membrane antigen [EMA] [p–r], and polyclonal carcinoembryonic antigen [pCEA] [s–u] in Area H-a, Area H-b and Area O). Arterial tumor vessels were positive for h-caldesmon (a–c). Negative immunostaining was observed (f,i,k,l,o). (p) "Cholangiole-like pattern" for EMA. (q,r) and (s,t,u) "cytoplasmic pattern" for EMA and pCEA, respectively.

positive if more than 1% of the tumor cells were stained.[16] Bmi-1 was defined as follows:[17] using the normal epithelium as an internal control, a diffuse distribution with a clear " 'dot-like' " staining pattern was scored as 2+; a focally distributed weak dot-like staining pattern was scored as 1+; and absence of any dot-like pattern was defined as negative. Ki-67 immunostaining was defined by selecting three hot spots (areas with the

highest density of immunostained nuclei), and adjacent cells were counted to include 100 nuclei. The average Ki-67 labeling index (Ki-67 LI) for the three areas was recorded as the percentage of positively stained tumor nuclei in 100 tumor cells. With regard to the expression EMA and pCEA, we examined the staining patterns of 50 tubules selected randomly in each area. If the expression was localized only on the surface of the glandular

lumen in an area of the same intensity as that of the cholangioles, the staining pattern was defined as "cholangiole-like", whereas if the expression was not confined to the surface of the granular lumen or when expression was seen in cytoplasm, the staining pattern was defined as "cytoplasmic". The ratio of this pattern in the 50 random tubules was evaluated three times, and the median value was used.

Statistical analysis

Unless otherwise indicated, numerical data are presented as the median (range). Differences in the proportions of categorical data were tested using the χ^2-test. Unless otherwise indicated, differences in the mean values of numerical data were tested using the two-tailed Mann–Whitney U-test. Overall survival was assessed using the Kaplan–Meier method. Differences were considered statistically significant at $P < 0.05$. All analyses were performed using the SPSS statistical software package (version 11.0.5; SPSS, Chicago, IL, USA).

RESULTS

Correlation between tumor enhancement and areal ratios of tumor cells and fibrous stroma

THE AREAL RATIOS of tumor cells and fibrous stroma were 71.6% (36.2–100%) and 28.4% (0–63.8%) in Area H-a, respectively ($P = 0.012$ and $P = 0.012$ vs Area O, respectively), 56.6% (18.8–84.4%) and 43.4% (15.6–81.2%) in Area H-b, respectively, and 33.1% (24.0–90.2%) and 66.9% (9.8–76.0%) in Area O, respectively. The areal ratio of tumor cells was high and that of fibrous stroma was low in Area H-a (Table 2, Figs 3A,4a).

Correlation between tumor enhancement, AVD and angiogenic factors

Arterial vessel density was 6.8 (3.6–18.2)/high-power (×200) field in Area H-a, 2.0 (0.8–4.6)/high-power (×200) field in Area H-b, and 2.5 (0–3.8)/high-power (×200) field in Area O (Table 2). AVD was therefore significantly higher in Area H-a than in Areas H-b and O ($P = 0.005$ and $P = 0.007$, respectively) (Fig. 4b).

Vascular endothelial growth factor was positive in six cases (75.0%) in Area H-a, five cases (62.5%) in Area H-b and one case (12.5%) in Area O (Table 2). The VEGF positivity rate was significantly higher in Areas H-a and H-b than in Area O ($P = 0.012$ and $P = 0.039$, respectively; Fig. 4c). Ang-2 was positive in eight cases

(100.0%) in Area H-a, seven cases (87.5%) in Area H-b, and 3 cases (37.5%) in Area O (Table 2). The Ang-2 positivity rate was significantly higher in Areas H-a and H-b than in Area O ($P = 0.007$ and $P = 0.0039$, respectively; Fig. 4c). Representative images of the h-caldesmon positive arteries and angiogenic factors are presented in Figure 3(B).

Association between tumor enhancement and biliary markers

Cytokeratin 7 was positive in all areas regardless of tumor enhancement. CK19 was positive in five cases (62.5%) in Area H-a, five cases (62.5%) in Area H-b and six cases (75.0%) in Area O (Table 2).

Correlation between tumor enhancement and stem cell features

Neural cell adhesion molecule was positive in six cases (75.0%) in Area H-a, two cases (25.0%) in Area H-b and one case (12.5%) in Area O (Table 2). The NCAM positivity rate was significantly higher in Area H-a than in Areas H-b and O ($P = 0.039$ and $P = 0.012$, respectively; Fig. 4d). The difference between Area H-b and Area O was not significant ($P = 0.552$). The final scores for Bmi-1 were as follows: six cases (75.0%) scored 2+ and two cases (25.0%) scored 1+ in Area H-a; three cases (37.5%) scored 2+ and five cases (62.5%) scored 1+ in Area H-b; and three cases (37.5%) scored 2+, four cases (50.0%) scored 1+ and one case (12.5%) scored 0+ in Area O (Table 2). No correlation was evident between the expression of SOX9, SOX17 or EpCAM and tumor enhancement.

Representative images of the NCAM and Bmi-1 are presented in Figure 3(B).

Correlation between tumor enhancement and malignancy evaluated by Ki-67 LI

The Ki-67 labeling index (LI) was 23.8% (4.3–56.3%) in Area H-a ($P = 0.046$ vs Area O), 26.0% (10.7–61.0%) in Area H-b and 52.2% (6.0–62.3%) in Area O (Table 2, Fig. 4e).

Correlation between tumor enhancement and staining patterns of EMA and pCEA

The proportion of tubules showing a cholangiole-like pattern of EMA was 57.0% (0–88%) in Area H-a, 9.0% (0–24%) in Area H-b and 0% (0–80%) in Area O (Table 2). Values were significantly higher in Area H-a than in Areas H-b and O ($P = 0.023$ and $P = 0.02$, respectively). The proportion of tubules showing a

Table 2 Histopathological and immunohistochemical findings in relation to enhancement patterns seen in the arterial phase of dynamic CT

		Area H-a (n = 8)	Area H-b (n = 8)	Area O (n = 8)
Microscopic area ratio	Median proportion of tumor cells (range)	71.6%† (36.2–100)	56.6% (18.8–84.4)	33.1% (24.0–90.2)
	Median proportion of fibrous stroma (range)	28.4%† (0–63.8)	43.4% (15.6–81.2)	66.9% (9.8–76.0)
AVD	Median AVD (range)	6.8‡ (3.6–18.2)	2.0 (0.8–4.6)	2.5 (0–3.8)
Immunohistochemical staining				
VEGF	Positive (proportion)	6† (75.0%)	5† (62.5%)	1 (12.5%)
Ang-2	Positive (proportion)	8§ (100%)	7† (87.5%)	3 (37.5%)
CK7	Positive (proportion)	8 (100%)	8 (100%)	8 (100%)
CK19	Positive (proportion)	5 (62.5%)	5 (62.5%)	6 (75.0%)
SOX9	Positive (proportion)	1 (12.5%)	0	1 (12.5%)
SOX17	Positive (proportion)	8 (100%)	8 (100%)	8 (100%)
EpCAM	Positive (proportion)	8 (100%)	7 (87.5%)	7 (87.5%)
NCAM	Positive (proportion)	6¶ (75.0%)	2 (25.0%)	1 (12.5%)
Bmi-1	2+/1+/0	6/2/0	3/5/0	3/4/1
Ki-67	Median proportion (range)	23.8%† (4.3–56.3)	26.0% (10.7–61.0)	52.2% (6.0–62.3)
EMA				
Cholangiole-like pattern	Median proportion (range)	57.0%¶ (0–88)	9.0% (0–24)	0% (0–80)
Cytoplasmic pattern	Median proportion (range)	41.0%†† (0–44)	81.0% (0–100)	93.0% (0–100%)
pCEA				
Cholangiole-like pattern	Median proportion (range)	0% (0–54)	0% (0–6)	0% (0–0)
Cytoplasmic pattern	Median proportion (range)	71.0% (28–100)	91.0% (0–100)	100.0% (96–100)

†$P < 0.05$ vs Area O.
‡$P < 0.01$ vs Areas H-b and O.
§$P < 0.01$ vs Area O.
¶$P < 0.05$ vs Areas H-b and O.
††$P < 0.01$ vs Area H-b and $P < 0.05$ vs. Area O.
Ang-2, angiopoietin-2; EpCAM; AVD, arterial vessel density; CK, cytokeratin; CT, computed tomography; EpCAM, epithelial cell adhesion molecule; NCAM, neural cell adhesion molecule; pCEA, polyclonal carcinoembryonic antigen; VEGF, vascular endothelial growth factor.
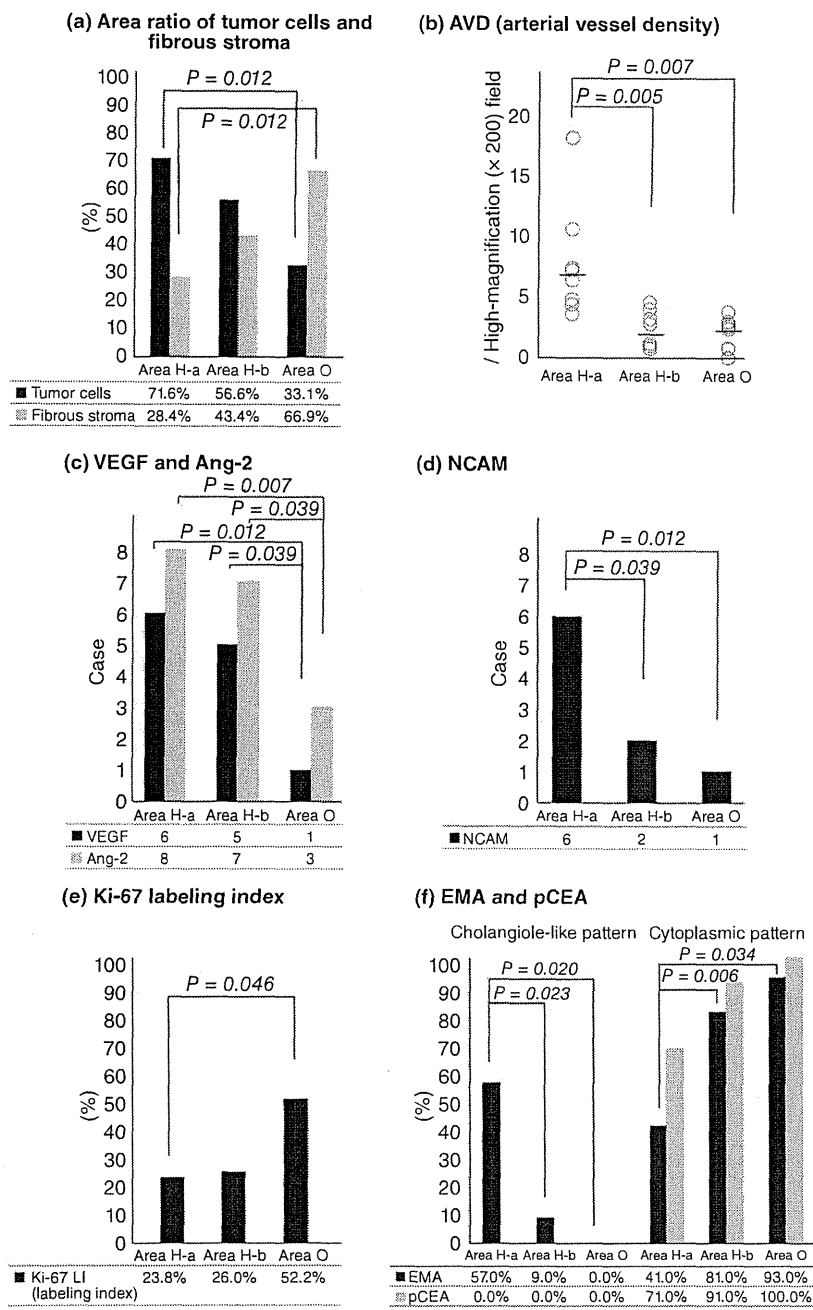
cytoplasmic pattern of EMA was 41.0% (0–44%) in Area H-a, 81.0% (0–100%) in Area H-b and 93.0% (0–100%) in Area O (Table 2). Values were significantly higher in Area H-b and O than in Area H-a ($P = 0.006$ and $P = 0.034$, respectively). The proportion of tubules showing a cholangiole-like pattern of pCEA was 0% (0–54%) in Area H-a, 0% (0–100%) in Area H-b and 0% in Area O. The proportion of tubules showing a cytoplasmic pattern of pCEA was 71.0% (28–100%) in Area H-a, 91.0% (0–100%) in Area H-b and 100.0% (96–100%) in Area O (Table 2). No significant differences between the groups were observed in the expressions of pCEA (Fig. 4e). Representative images of the EMA and pCEA are presented in Figure 3(B).

Postoperative data

The 5-year postoperative survival rate was 87.5% for patients with h-CCC and 62.5% for patients with o-CCC. Intrahepatic recurrence was detected in three cases with h-CCC, all of which were hypervascular. Hypovascular intrahepatic recurrence occurred in one case with o-CCC. Detailed postoperative data is summarized in Table S1.

DISCUSSION

MOST CCC ARE hypovascular but some are reported to be hypervascular.[4,5] Hypervascular CCC is reported to have better prognosis than

(a) Area ratio of tumor cells and fibrous stroma

	Area H-a	Area H-b	Area O
■ Tumor cells	71.6%	56.6%	33.1%
▒ Fibrous stroma	28.4%	43.4%	66.9%

(b) AVD (arterial vessel density)

(c) VEGF and Ang-2

	Area H-a	Area H-b	Area O
■ VEGF	6	5	1
▒ Ang-2	8	7	3

(d) NCAM

	Area H-a	Area H-b	Area O
■ NCAM	6	2	1

(e) Ki-67 labeling index

	Area H-a	Area H-b	Area O
■ Ki-67 LI (labeling index)	23.8%	26.0%	52.2%

(f) EMA and pCEA

	Cholangiole-like pattern			Cytoplasmic pattern		
	Area H-a	Area H-b	Area O	Area H-a	Area H-b	Area O
■ EMA	57.0%	9.0%	0.0%	41.0%	81.0%	93.0%
▒ pCEA	0.0%	0.0%	0.0%	71.0%	91.0%	100.0%

Figure 4 Results of statistical analyses of histopathological data. (a) Areal ratio of tumor cells and fibrous stroma in each area. (b) Distribution of arterial vessel density (AVD) (/high-power [×200] field) in each area. (c) Positivity for angiogenic factors in each area. (d) Positivity for neural cell adhesion molecule (NCAM) in each area. (e) Ki-67 labeling index in each area. (f) The proportion of tubules demonstrating a cholangiole-like pattern and a cytoplasmic pattern of epithelial membrane antigen (EMA) and polyclonal carcinoembryonic antigen (pCEA) in each area. (a) ■, tumor cells; ▒, fibrous stroma; (c) ■, vascular endothelial growth factor (VEGF); ▒, angiopoietin-2 (Ang-2); (d) ■, NCAM; (e) ■, Ki-67 LI (labeling index); (f) ■, EMA; ▒, pCEA.

hypovascular CCC. This study was conducted to examine histopathological features of hypervascular CCC, which remain to be fully clarified, and to establish objective and reproducible radiological definitions for the same.

The results of this histopathological study indicated that the following factors reflected tumor enhancement: a high areal ratio of tumor cells, a low areal ratio of fibrous stroma and a high AVD. Results for the first two factors provided confirmation of those in previous

reports,[9,18] but no previous study has attempted quantitative evaluation using an image processing software.

The relationship between tumor enhancement and mean vessel density (MVD) in CCC has been investigated previously. Some studies observed a correlation,[10] whereas others failed to demonstrate any relationship.[2] As MVD includes all capillary vessels, including non-arterial vessels, it does not accurately reflect tumor enhancement in the arterial phase of dynamic CT. Therefore, AVD rather than MVD was examined and calculated by staining arterial vessels for h-caldesmon, which is specific for arterial vessel smooth muscle. Aishima *et al.* adopted a similar approach,[14] but did not refer to the correlation between AVD and tumor enhancement. In this study, AVD was significantly higher in Area H-a than in Areas H-b and O. Therefore, AVD appears to be a factor that directly reflects tumor enhancement of CCC.

In terms of IHC analysis, no previous study has addressed the relationship between angiogenic factors and tumor enhancement in CCC. In this study, expressions of both the angiogenic factors VEGF and Ang-2 were not always significantly correlated with enhancement in the arterial phase of dynamic CT. In Area H-b, a discrepancy was observed between low AVD (reflecting hypovascularity upon imaging) and high expressions of VEGF and Ang-2. Tumor cells may strongly express angiogenic factors in Area H-b as well as in Area H-a; however, the low areal ratio of tumor cells and high areal ratio of fibrous stroma resulted in a decline of AVD, as reflected by hypovascularity upon imaging.

In this study, the correlation between tumor enhancement and malignant potential was evaluated by IHC measurement of the Ki-67 LI. The Ki-67 LI has recently been used as an index of grade, vessel invasion, lymph node metastasis and prognosis of many cancers.[19-22] From the results of Ki-67 LI, we observed low malignancy in tumor cells in Area H-a and increasing malignant potential in the following order: Area H-a, Area H-b and Area O.

Expressions of the stem cell markers NCAM, Bmi-1, SOX9, SOX17 and EpCAM varied among cases, but significant differences were observed in the expressions of NCAM between h-CCC and o-CCC patients. NCAM is expressed in relatively primitive cholangiocytes, and its expression gradually diminishes over time.[23] NCAM is considered to be a marker of hepatic progenitor cells and is expressed in primitive cells in the liver.[16] Overexpression of Bmi-1 RNA has been reported in CCC and is considered to be related to the stem cell-like properties of this tumor.[24] In the present study, expression of NCAM was significantly higher, and that of Bmi-1 tended to be higher in Area H-a. We think the types and combinations in expressions of stem cell markers varied among cases according to Kim *et al.*'s report[25] which examined IHC stain of hepatocellular carcinoma in relation to four stemness-related genes and the types and combinations in expressions of stem cell markers varied among cases. Therefore, tumor cells in hypervascular areas may have stem cell-like features.

These results suggested that h-CCC may progresses to CCC composed of hypervascular components (such as those found in Area H-a) and hypovascular components (such as those found in Area H-b) as the amount of fibrous stroma increases and the number of arterial vessels decreases. In addition, the arterial phase of dynamic CT reveals the less malignant component as a hypervascular area. In previous histological reports, an association was found between a high degree of fibrosis and poor differentiation in CCC,[2] and a decrease in the number of intratumoral arteries reflected tumor aggression.[14] From a clinical viewpoint, prognosis of patients with h-CCC tended to be better than that of patients with o-CCC, reflecting the results of previous reports.[5,10] In this study, the 5-year survival rate of patients with h-CCC was superior to that of patients with o-CCC. h-CCC can thus be interpreted as a less malignant tumor than o-CCC from both clinical and pathological points of view.

From the results of EMA expression, the proportion of tubules showing a cholangiole-like pattern was significantly higher in Area H-a than in Area H-b and O. Therefore, it may be a useful marker of h-CCC. Komuta *et al.* have reported that the intraluminal staining pattern of pCEA is specific to CoCC.[16] Thus, h-CCC and CoCC appear to share some common features in terms of tumor enhancement[11] and stem cell features.[16] However, not all of the histopathological features of Area H-a observed were typical of CoCC (data not shown), and had specific characteristics of cancer cells on HE staining. High-attenuation area in o-CCC was small; therefore, detailed examination of histopathological findings in o-CCC was difficult to evaluate.

In conclusion, this study identified high areal ratios of tumor cells and AVD as well as high expressions of stem cell and angiogenic markers in h-CCC, whereas both the areal ratio of fibrous stroma and the Ki-67 LI values were low. A decrease in stem cell markers along with an increase of pathological malignant potential, increase of fibrous stroma and a decrease of AVD, reflecting tumor enhancement upon imaging, are also characteristic of this process. Therefore, heterogeneity of enhancement

© 2013 The Japan Society of Hepatology

and pathology in h-CCC may reflect the process of stepwise carcinogenesis from early CCC to o-CCC. The 5-year survival rate in cases of h-CCC is better than in cases of o-CCC. These results suggested that h-CCC is less malignant and more premature component than o-CCC from both clinical and pathological aspects, which may represents an early stage of CCC.

ACKNOWLEDGMENTS

REFERENCES

1 Khan SA, Thomas HC, Davidson BR, Taylor-Robinson SD. Cholangiocarcinoma. *Lancet* 2005; 366: 1303–14.
2 Nanashima A, Sumida Y, Abo T *et al.* Relationship between pattern of tumor enhancement and clinicopathologic characteristics in intrahepatic cholangiocarcinoma. *J Surg Oncol* 2008; 98: 535–9.
3 Honda H, Onitsuka H, Yasumori K *et al.* Intrahepatic peripheral cholangiocarcinoma: two-phased dynamic incremental CT and pathologic correlation. *J Comput Assist Tomogr* 1993; 17: 397–402.
4 Yamamoto M, Ariizumi S, Otsubo T *et al.* Intrahepatic cholangiocarcinoma diagnosed preoperatively as hepatocellular carcinoma. *J Surg Oncol* 2004; 87: 80–3; discussion 83–4.
5 Kim SA, Lee JM, Lee KB *et al.* Intrahepatic mass-forming cholangiocarcinomas: enhancement patterns at multiphasic CT, with special emphasis on arterial enhancement pattern-correlation with clinicopathologic findings. *Radiology* 2011; 260: 148–57.
6 Fan ZM, Yamashita Y, Harada M *et al.* Intrahepatic cholangiocarcinoma: spin-echo and contrast-enhanced dynamic MR imaging. *AJR Am J Roentgenol* 1993; 161: 313–17.
7 Kim TK, Choi BI, Han JK, Jang HJ, Cho SG, Han MC. Peripheral cholangiocarcinoma of the liver: two-phase spiral CT findings. *Radiology* 1997; 204: 539–43.
8 Zhang ZL, Liu ZS, Sun Q. Expression of angiopoietins, Tie2 and vascular endothelial growth factor in angiogenesis and progression of hepatocellular carcinoma. *World J Gastroenterol* 2006; 12: 4241–5.
9 Zhang Y, Uchida M, Abe T, Nishimura H, Hayabuchi N, Nakashima Y. Intrahepatic peripheral cholangiocarcinoma: comparison of dynamic CT and dynamic MRI. *J Comput Assist Tomogr* 1999; 23: 670–7.
10 Ariizumi SI, Kotera Y, Takahashi Y *et al.* Mass-forming intrahepatic cholangiocarcinoma with marked enhancement on arterial-phase computed tomography reflects

11 Asayama Y, Tajima T, Okamoto D *et al.* Imaging of cholangiolocellular carcinoma of the liver. *Eur J Radiol* 2009; 75: 120–5.
12 Bosman FT, Carneiro F, Hruban RH, Theise ND. *WHO Classification of Tumours of the Digestive System: International Agency for Research on Cancer.* IARC: Lyon, 2010.
13 Loyer EM, Chin H, DuBrow RA, David CL, Eftekhari F, Charnsangavej C. Hepatocellular carcinoma and intrahepatic peripheral cholangiocarcinoma: enhancement patterns with quadruple phase helical CT-a comparative study. *Radiology* 1999; 212: 866–75.
14 Aishima S, Iguchi T, Nishihara Y *et al.* Decreased intratumoral arteries reflect portal tract destruction and aggressive characteristics in intrahepatic cholangiocarcinoma. *Histopathology* 2009; 54: 452–61.
15 Yoshikawa D, Ojima H, Iwasaki M *et al.* Clinicopathological and prognostic significance of EGFR, VEGF, and HER2 expression in cholangiocarcinoma. *Br J Cancer* 2008; 98: 418–25.
16 Komuta M, Spee B, Vander Borght S *et al.* Clinicopathological study on cholangiolocellular carcinoma suggesting hepatic progenitor cell origin. *Hepatology* 2008; 47: 1544–56.
17 Effendi K, Mori T, Komuta M, Masugi Y, Du W, Sakamoto M. Bmi-1 gene is upregulated in early-stage hepatocellular carcinoma and correlates with ATP-binding cassette transporter B1 expression. *Cancer Sci* 2010; 101: 666–72.
18 Murakami T, Nakamura H, Tsuda K *et al.* Contrast-enhanced MR imaging of intrahepatic cholangiocarcinoma: pathologic correlation study. *J Magn Reson Imaging* 1995; 5: 165–70.
19 Johannessen AL, Torp SH. The clinical value of Ki-67/MIB-1 labeling index in human astrocytomas. *Pathol Oncol Res* 2006; 12: 143–7.
20 Stuart-Harris R, Caldas C, Pinder SE, Pharoah P. Proliferation markers and survival in early breast cancer: a systematic review and meta-analysis of 85 studies in 32,825 patients. *Breast* 2008; 17: 323–34.
21 Oya M, Yao T, Nagai E, Tsuneyoshi M. Metastasizing intramucosal gastric carcinomas. Well differentiated type and proliferative activity using proliferative cell nuclear antigen and Ki-67. *Cancer* 1995; 75: 926–35.
22 Munstedt K, von Georgi R, Franke FE. Correlation between MIB1-determined tumor growth fraction and incidence of tumor recurrence in early ovarian carcinomas. *Cancer Invest* 2004; 22: 185–94.
23 Nakanuma Y, Sasaki M, Ikeda H *et al.* Pathology of peripheral intrahepatic cholangiocarcinoma with reference to tumorigenesis. *Hepatol Res* 2008; 38: 325–34.
24 Sasaki M, Yamaguchi J, Ikeda H, Itatsu K, Nakanuma Y. Polycomb group protein Bmi1 is overexpressed and essential in anchorage-independent colony formation,

cell proliferation and repression of cellular senescence in cholangiocarcinoma: tissue and culture studies. *Hum Pathol* 2009; 40: 1723–30.

25 Kim H, Choi GH, Na DC *et al.* Human hepatocellular carcinomas with "Stemness"-related marker expression: keratin 19 expression and a poor prognosis. *Hepatology* 2011; 54: 1707–17.

SUPPORTING INFORMATION

ADDITIONAL SUPPORTING INFORMATION may be found in the online version of this article at the publisher's website:

Table S1 Detailed clinicopathological data for patients with hypervascular cholangiocellular carcinoma (h-CCC) and ordinary hypovascular CCC (o-CCC).

Table S2 Detailed data of attenuation values in each area.

Table S3 Details of the primary antibodies used in this study.

Contents lists available at ScienceDirect

Developmental Biology
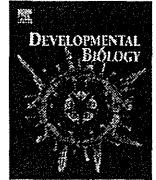
Gene expression ontogeny of spermatogenesis in the marmoset uncovers primate characteristics during testicular development

CrossMark

Zachary Yu-Ching Lin [a], Takamasa Hirano [b], Shinsuke Shibata [a], Naomi M. Seki [b,c], Ryunosuke Kitajima [d], Ayako Sedohara [e], Mikiko C. Siomi [b,c], Erika Sasaki [a,e,f], Haruhiko Siomi [b], Masanori Imamura [a,d,*], Hideyuki Okano [a,**]

[a] Department of Physiology, School of Medicine, Keio University, 35 Shinanomachi, Shinjuku-ku, Tokyo 160-8582, Japan
[b] Department of Molecular Biology, School of Medicine, Keio University, 35 Shinanomachi, Shinjuku-ku, Tokyo 160-8582, Japan
[c] Department of Biological Sciences, Graduate School of Science, The University of Tokyo, 7-3-1 Hongo, Bunkyo-ku, Tokyo 113-0033, Japan
[d] Molecular Biology Section, Department of Cellular and Molecular Biology, Primate Research Institute, Kyoto University, Inuyama, Aichi 484-8506, Japan
[e] Department of Applied Developmental Biology, Central Institute for Experimental Animals, 3-25-12 Tonomachi, Kawasaki 210-0821, Japan
[f] PRESTO Japan Science and Technology Agency, Japan

ARTICLE INFO

ABSTRACT

Mammalian spermatogenesis has been investigated extensively in rodents and a strictly controlled developmental process has been defined at cellular and molecular levels. In comparison, primate spermatogenesis has been far less well characterized. However, important differences between primate and rodent spermatogenesis are emerging so it is not always accurate to extrapolate findings in rodents to primate systems. Here, we performed an extensive immunofluorescence study of spermatogenesis in neonatal, juvenile, and adult testes in the common marmoset (Callithrix jacchus) to determine primate-specific patterns of gene expression that underpin primate germ cell development. Initially we characterized adult spermatogonia into two main classes; mitotically active C-KIT$^+$Ki67$^+$ cells and mitotically quiescent SALL4$^+$PLZF$^+$LIN28$^+$DPPA4$^+$ cells. We then explored the expression of a set of markers, including PIWIL1/MARWI, VASA, DAZL, CLGN, RanBPM, SYCP1 and HAPRIN, during germ cell differentiation from early spermatocytes through round and elongating spermatids, and a clear program of gene expression changes was determined as development proceeded. We then examined the juvenile marmoset testis. Markers of gonocytes demonstrated two populations; one that migrates to the basal membrane where they form the SALL4$^+$ or C-KIT$^+$ spermatogonia, and another that remains in the lumen of the seminiferous tubule. This later population, historically identified as pre-spermatogonia, expressed meiotic and apoptotic markers and were eliminated because they appear to have failed to correctly migrate. Our findings provide the first platform of gene expression dynamics in adult and developing germ cells of the common marmoset. Although we have characterized a limited number of genes, these results will facilitate primate spermatogenesis research and understanding of human reproduction.

© 2015 Elsevier Inc. All rights reserved.

Introduction

Mammalian spermatogenesis is a strictly organized developmental process involved in the passage of genetic material. Spermatogenesis originates from a population of spermatogonia called spermatogonial stem cells that undergo the sequential processes of mitotic and meiotic spermiogenesis to produce spermatozoa. In rodents, many aspects of spermatogenesis have been analyzed including cell morphology, organization, and gene expression (Hermo et al., 2010). These studies have led to the identification of numerous molecular signatures to discriminate each stage of spermatogenesis. By contrast, owing to less accessibility to tissue samples and ethical and legal issues, there are fewer such comparative studies on primate spermatogenesis.

An increasing number of studies have revealed that primates and rodents have a different developmental program for spermatogenesis (YDBIOI6681Hermann et al., 2010; McKinnell et al., 2013; Schlatt and Ehmcke, 2014). For example, the stem cell system underlying spermatogenesis differs between primates and rodents. In humans there are two distinct types of undifferentiated spermatogonia; quiescent A_{dark} spermatogonia, which are

believed to serve as reserve stem cells, and renewing A_{pale} spermatogonia, which proliferate regularly (YDBIOl 6681Clermont, 1963, 1966, 1969, 1972). This categorization is also the case in New-World (YDBIOl6681Eildermann et al., 2012; Millar et al., 2000) and Old-World monkeys (YDBIOl6681Ehmcke et al., 2006; Hermann et al., 2010), but is not incorporated into rodent spermatogenesis that does not enclose reserve stem cells (Schlatt and Ehmcke, 2014).

Differences in the molecular profile are also evident between primate and rodent spermatogenesis. In our previous study, we compared the molecular signatures of spermatogenic cells in mouse and common marmoset (*Callithrix jacchus*) with regard to DNA methylation status, transcripts, and protein expression (Lin et al., 2012). We revealed that in marmosets the *NANOG* and *OCT4* promoters exhibit DNA hypomethylation and hypermethylation, respectively, unlike mouse homologs, which display an opposite DNA methylation pattern (YDBIOl6681Imamura et al., 2006; Western et al., 2010). Additionally, we found that marmoset spermatogonia express DAZL but not VASA protein, while both proteins are expressed in mouse spermatogonia. These observations reveal that simple extrapolation of rodent insights to primates is not appropriate. Hence, investigation of primates should be considered. However, very little is known about the molecular dynamics of primate spermatogenesis. There is, therefore, a fundamental need for a suitable non-human primate model.

As a model animal to investigate primate spermatogenesis, we have focused on a New-World monkey, the common marmoset that is native to the Atlantic coastal forests in northeastern Brazil. Among primates this species has attracted much attention in recent years as it is an excellent experimental animal for biomedical research. It has a small body size (20–30 cm height; 350–400 g weight in adulthood), fast sexual maturation (around 1.5 years old), breeds throughout the year with a prolificacy of 40–80 offspring for a female life, and is physiologically similar to humans (YDBIOl 6681Kishi et al., 2014; Mansfield, 2003; Okano et al., 2012). In addition, our group has succeeded in producing offspring with assisted reproduction technologies (YDBIOl6681Takahashi et al., 2014, Tomioka et al., 2012), and creating a transgenic marmoset with germline transmission (Sasaki et al., 2009), expanding their potential for genetic research. Furthermore, compared with other non-human primates, marmosets and humans share a similar organization of spermatogenesis and testicular development (YDBIOl6681Millar et al., 2000; Mitchell et al., 2008; Saunders et al., 1996; Wistuba et al., 2003) as both species retain gonocytes in the postnatal testes (YDBIOl6681Albert et al., 2010; Sharpe et al., 2003). To date, some studies have examined gene expression of marmoset germ cells but only focused on either a single or a few genes (e.g. OCT4, SALL4, and VASA) at a particular developmental stage (YDBIOl6681Eildermann et al., 2012; Lin et al., 2012; McKinnell et al., 2013). A comprehensive gene expression atlas of marmoset spermatogenesis remains to be defined.

In this study, to develop the atlas of gene expression dynamics in the course of marmoset spermatogenesis, we dissected a sequence of gene expression associated with spermatogenic processes. Extensive immunofluorescent microscopy of neonatal, juvenile, and adult testes elucidated not only gene expression benchmarks but also a unique developmental event occurring in the juvenile period. We believe that our findings could serve as the first molecular platform to facilitate primate spermatogenesis research, and be a first step for unveiling primate-specific developmental programs.

Materials and methods

Animals and tissue collection

All the common marmosets used in this study were housed in cages with dimensions of $82 \times 61 \times 160\ cm^3$. This study was approved by Institutional Animal Care and Use Committee of the Central for Experimental Animals (CIEA) and was performed in accordance with CIEA guidelines that agree with the Guidelines for Proper Conduct of Animal Experiments by the Science Council of Japan (2006).

RT-PCR

Total RNA prepared with TRIzol reagent was isolated using the RNeasy Mini kit (Qiagen, 74106) according to the manufacturer's instructions. First-strand cDNA was synthesized with SuperScriptIII reverse transcriptase (Invitrogen, 18080-044) and oligo-dT$_{18}$ primer. The primers were designed based on sequences in the marmoset genome database (http://genome.wustl.edu/tools/blast/index) as described in Supplementary Table S1. Subsequent PCR analysis was performed with Ex Taq Hot Start Version (TaKaRa, RR006A). All experiments were performed semiquantitatively at three different escalation cycles, and only representative images are shown in the result.

Western blot

Marmoset tissues were homogenized in lysis buffer containing 20 mM Tris–HCl (pH 8.0), 150 mM NaCl, 2 mM EDTA (pH 8.0) and 1% Nonidet-P40 (NP-40). After centrifugation, the supernatants were diluted with sample buffer and boiled. Ten microgram of total proteins per lean was separated on 7.5% SDS-PAGE and transferred nitrocellulose (Whatman, 10 401 196) or PVDF (GE Healthcare, RPN303F) membranes. The membranes were blocked at room temperature with 5% (w/v) skim milk for 30 min. After five washes with 0.1% PBS-T, the membranes were incubated with primary antibodies at room temperature for 1 h or overnight at 4 °C. The following primary antibodies were used: culture supernatant of anti-MARWI hybridoma cells (1:1, 2D9) (Hirano et al., 2014), anti-GST (1:1000, Santa Cruz Biotechnology, sc-138), anti-FLAG (M2) (1:5000, Sigma, F3165), anti-GAPDH (14C10) (1:3000, Cell Signaling, 2118) antibodies. HRP-conjugated anti-mouse IgG (1:5000, MP BIOMEDICALS, 55558) or anti-rabbit IgG (1:5000, Immuno-Biological Laboratories, 17502) were used as secondary antibodies. Blots were developed using ECL detection reagents (Amersham Biosciences, RPN2109).

Immuno-electron microscopy

Frozen sections from adult marmoset testes were incubated with anti-MARWI antibody (1:200, 2D9-1H6) for 4 days at 4 °C followed by incubation with nanogold conjugated anti-mouse secondary antibody (1:100, Invitrogen, A-24921) for 1 day at 4 °C. After fixation in 2.5% glutaraldehyde for 10 min and enhancement with HQ-Silver enhancement kit (Nanoprobes Inc., 2012) for 12 min at 25 °C in a dark room, sections were post-fixed with 0.5% osmium tetroxide, dehydrated through ethanol, acetone, and QY1, and embedded in Epon. Ultrathin sections (70 nm thickness) were prepared and stained with 2% uranyl acetate and 80 mM lead citrate (Reynolds methods) for 15 and 10 min respectively. The sections were observed under a transmission electron microscope (JEOL model 1230), while images were taken with a Digital Micrograph 3.3 (Gatan Inc.).

Immunofluorescence microscopy of marmoset testis

Testes were isolated from neonatal (1-day-old), juvenile (10-month-old), and adult marmosets (2, 3, 4, 5, 9, 10-year-old). Each testis was fixed in 4% (w/v) paraformaldehyde, dehydrated, embedded in paraffin wax and sectioned at 5 μm thickness. The sections were de-waxed with xylene, rehydrated in a graded alcohol series, and washed with distilled water. For immunofluorescence analyses, the sections were subjected to antigen retrieval by autoclave at 105 °C for at least 5 min in 1 × Target Retrieval Solution (Dako, S1699). The sections were blocked at room temperature with 5% (w/v) skim milk for 30 min and incubated with the primary antibody at 4 °C overnight in a humidified chamber. The following primary antibodies were used: rabbit anti-SALL4 (1:100, Abcam, ab29112), mouse anti-SALL4 (1:100, Abcam, ab57577), rabbit anti-Ki67 (1:100, Leica Biosystems, NCL-Ki67p), mouse anti-Ki67 (1:100, Leica Biosystems, NCL-L-Ki67-MM1), rabbit anti-C-KIT (1:100, Abcam, ab32363), mouse anti-PLZF (1:100, Abcam, ab104854), goat anti-LIN28A (1:100, R&D systems, AF3757), rabbit anti-DPPA4 (1:50, Abcam, ab154642), mouse anti-MARWI (1:50, 2D9-1H6), rabbit anti-DDX4 (1:50, Abcam, ab13840), mouse anti-DDX4 (1:50, Abcam, ab27591), rabbit anti-DAZL (1:100, Abcam, ab34139), rabbit anti-Calmegin (1:100, Abcam, ab171971), rabbit anti-RanBPM (1:100, Abcam, ab78127), rabbit anti-SYCP1 (1:100, Abcam, ab15087), goat anti-RNF98 (1:100, Abcam, ab4836), mouse anti-phospho-histone H2A. X (ser139) (1:100, Millipore, 05-636), rabbit anti-active Caspase 3 (1:100, Abcam, ab13847), and rabbit anti-PARP1(Asp214) (1:100, Cell Signaling, 9541S) antibodies. Secondary antibodies included Alexa Fluor 488 goat anti-mouse IgG (1:500; Invitrogen, A-11029), Alexa Flour 488 donkey anti-mouse IgG (1:500, Invitrogen, A-21202), Alexa Flour 488 donkey anti-goat IgG (1:500, Invitrogen, A-11055), Alexa Fluor 555 goat anti-rabbit IgG (1:500, Invitrogen, A-21429), Alexa Flour 555 donkey anti-rabbit IgG (1:500, Invitrogen, A-31572), and Alexa Flour 555 donkey anti-goat IgG (1:500, Invitrogen, A-21432). Nuclei were stained with 10 ng/ml Hoechst 33342. For each experiment, a negative control was included in which the primary antibody had been omitted. Images were captured using a Zeiss confocal microscope system (LSM700).

Results

Molecular subtyping of spermatogonia in adult marmoset testis

The common marmoset has two subtypes of undifferentiated A spermatogonia; one is mitotically quiescent A_{dark} spermatogonia, and the other is mitotically active A_{pale} spermatogonia (YDBIOI6681Hermann et al., 2010; Millar et al., 2000). These two types of spermatogonia have been classically recognized by their characteristic nuclear staining patterns and morphological criteria, but their molecular signatures remain unclear. To discriminate marmoset spermatogonia subtypes by gene expression, we carried out immunofluorescence analyses of adult marmoset testes, referring to known spermatogonia markers in other mammalian species. First, we focused on the Ki67 antigen, an indicator for dividing cells (Gerdes et al., 1984), because the major cytological difference between A_{dark} and A_{pale} spermatogonia is their mitotic activity (YDBIOI6681Dym et al., 2009; Ehmcke and Schlatt, 2006). The distribution of Ki67$^+$ cells in the seminiferous tubules was compared with cells expressing pluripotency transcription factor SALL4, which is known to be a type A spermatogonium marker (Eildermann et al., 2012). Although both SALL4 and Ki67 were detected in marmoset spermatogonia, the SALL4$^+$ and Ki67$^+$ spermatogonia clearly constituted different populations (Fig. 1A and Supplementary Fig. S1).

We next examined the expression of C-KIT protein, which is also known to mark spermatogonia in marmosets (von Schonfeldt et al., 1999) and rhesus macaques (Hermann et al., 2009). C-KIT protein was mostly expressed in the Ki67$^+$ spermatogonia, albeit a part of C-KIT$^+$ spermatogonia did not display Ki67 staining (Fig. 1B and Supplementary Fig. S2). By contrast, the expression of SALL4 and C-KIT proteins seemed to be mutually exclusive (Fig. 1C) while other spermatogonial markers, PLZF (YDBIOI6681Hermann et al., 2007; Hermann et al., 2009) and LIN28 (Aeckerle et al., 2012) proteins, were basically co-expressed with SALL4 protein (Fig. 1D and E), which is similar to the case of mouse homologs (YDBIOI 6681Gassei and Orwig, 2013; Hobbs et al., 2012). DPPA4 (Maldonado-Saldivia et al., 2007) protein was also specified in the SALL4$^+$ spermatogonia (Fig. 1F). Taken together, it seems that marmoset spermatogonia can be classified into two major subtypes, which are SALL4$^+$PLZF$^+$LIN28$^+$DPPA4$^+$ mitotically quiescent cells, and C-KIT$^+$Ki67$^+$ mitotically active cells, possibly suggesting A_{dark} and A_{pale} spermatogonia respectively.

Marmoset PIWIL1, a component of chromatoid body

Next, we were interested in identifying gene expression of the spermatocytes and spermatids in adult marmoset testis. We have already found that germ cell-specific RNA helicase VASA is expressed from primary spermatocytes to round spermatids (Lin et al., 2012); hence, we intended to examine the expression of other marker genes. We particularly focused on the PIWI-family proteins, which associate with PIWI-interacting RNAs (piRNAs) to protect genomic integrity from transposable elements and, therefore, are expected to be conserved across mammalian species (Siomi et al., 2011). RT-PCR analysis of marmoset tissues identified the expression of all four PIWI genes (*PIWIL1, 2, 3*, and *4*) in testis together with the related genes (Supplementary Fig. S3), as reported in humans (Sasaki et al., 2003). Among them, PIWIL1 was subjected to detailed investigation because mouse PIWIL1/MIWI is expressed from pachytene spermatocytes to the elongating spermatids (Deng and Lin, 2002) and interacts with VASA protein (Kuramochi-Miyagawa et al., 2004).

To examine the expression of marmoset homologue of PIWIL1, which we designated as MARWI, we utilized an anti-MARWI monoclonal antibody derived from a hybridoma line 2D9 (Supplementary Fig. S4) (Hirano et al., 2014). In mice, PIWIL1/MIWI protein is concentrated in the chromatoid body, a germ cell-specific cloud-shaped granule, together with VASA protein in the cytoplasm of pachytene spermatocytes and spermatids (Kotaja and Sassone-Corsi, 2007). We carried out immunofluorescence analysis of marmoset testis and found that the subcellular localization of MARWI protein corresponded to that of VASA protein (Fig. 2A), in accordance with our recent report (Hirano et al., 2014). Notably, large granular staining of MARWI and VASA proteins was clearly observed in the round spermatids. The localization of MARWI protein was further examined by immuno-electron microscopy that identified marmoset chromatoid bodies with high electron density, in which MARWI protein was incorporated (Fig. 2B).

Molecular staging of marmoset spermatogenesis from spermatocytes to spermatids

To characterize developmental stage-specific gene expression in marmoset spermatocytes and spermatids, we examined MARWI protein in combination with other germ cell-related genes. As reported previously (YDBIOI6681Lin et al., 2012; Ruggiu et al., 2000), an RNA-binding protein DAZL was expressed in marmoset spermatogonia and spermatocytes (Fig. 3A). By contrast, MARWI protein appeared at the pachytene spermatocyte stage and the expression continued throughout the round and elongating
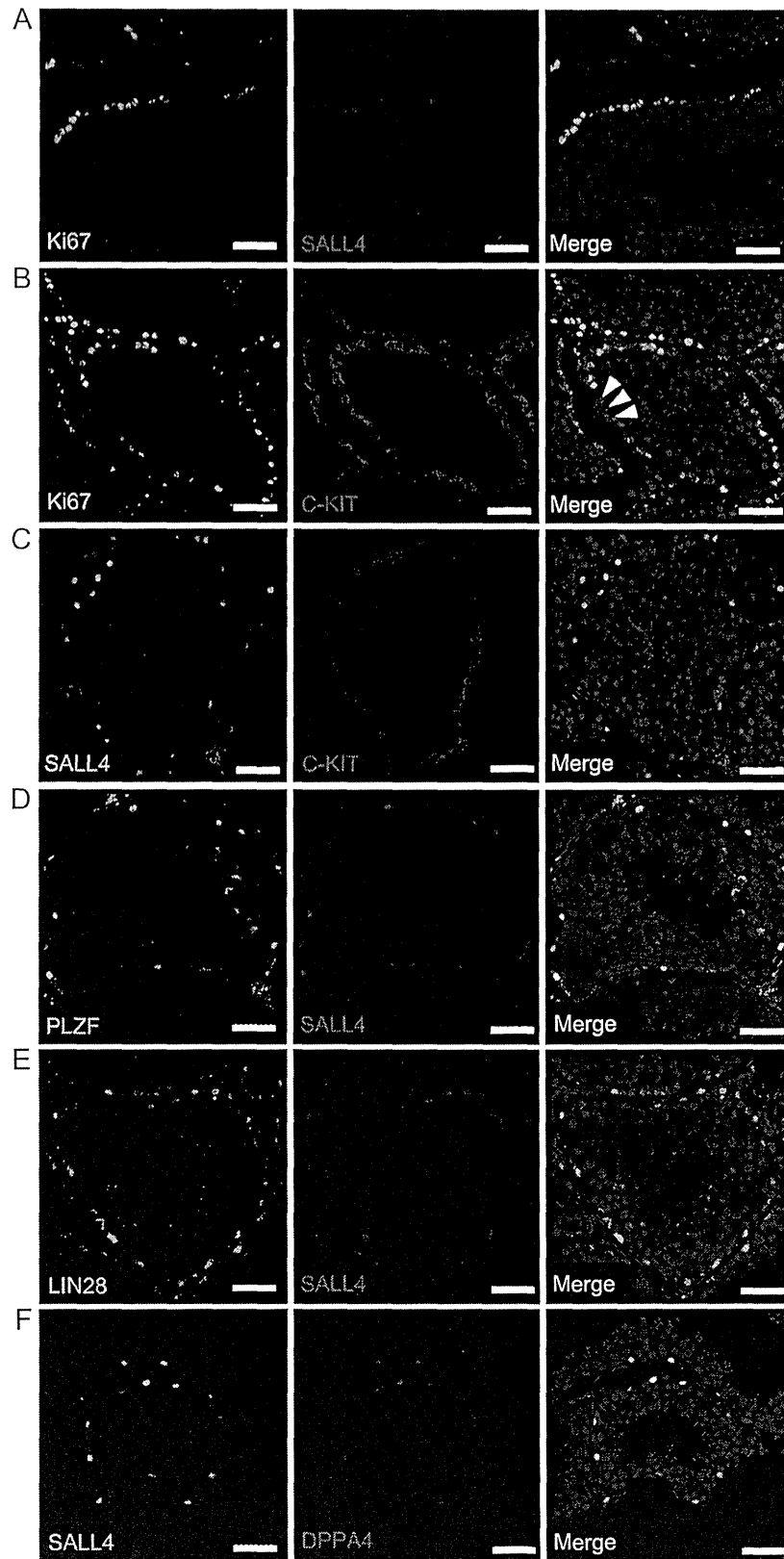
Fig. 1. Spermatogonial subtypes in the adult marmoset testis. Confocal images of adult marmoset testis sections co-stained with antibodies against spermatogonial markers, including (A) anti-Ki67 and anti-SALL4 antibodies, (B) anti-Ki67 and anti-C-KIT antibodies, (C) anti-SALL4 and anti-C-KIT antibodies, (D) anti-PLZF and anti-SALL4 antibodies, (E) anti-LIN28 and anti-SALL4 antibodies, and (F) anti-SALL4 and anti-DPPA4 antibodies. In the image of (B), arrowheads indicate C-KIT$^+$Ki67$^-$ spermatogonia. Nuclei were counterstained with Hoechst 33342. Scale bar, 50 μm.

A

B
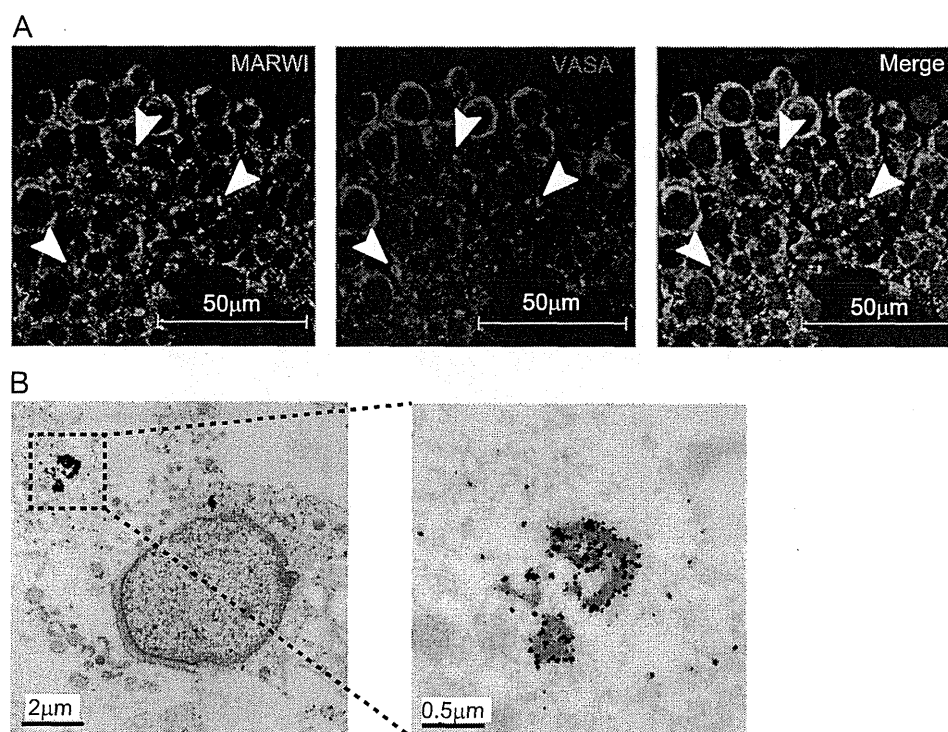
Fig. 2. Subcellular localization of marmoset PIWIL1 protein in chromatoid body. (A) Confocal images of adult testis frozen sections co-stained with anti-MARWI and anti-VASA antibodies. Arrowheads indicate chromatoid body-like cytoplasmic granules consisted of condensed MARWI and VASA proteins. Nuclei were counterstained with Hoechst 33342. Scale bar, 50 μm. (B) Immuno-electron microscopic analysis of adult testis frozen section stained with anti-MARWI antibody. MARWI proteins were detected in chromatoid bodies with high electron density in the cytoplasm.

spermatid stages; therefore only the pachytene spermatocytes expressed both proteins. During mouse spermatogenesis, a testis-specific chaperone protein Calmegin (CLGN) is expressed in the pachytene spermatocytes to the elongating spermatids, and disappears in the mature spermatids (Yoshinaga et al., 1999). Marmoset CLGN protein first appeared in the early spermatocytes modestly, and then culminated at the pachytene spermatocyte stage in accordance with the onset of MARWI expression (Fig. 3B). The expression was also observed in the round spermatids but not in the elongating spermatids.

The expression of VASA and MARWI proteins mostly overlapped during the course of marmoset spermatogenesis as both proteins were expressed in the pachytene spermatocytes to the round spermatids (Fig. 3C). However, in the elongating spermatids, MARWI, but not VASA, was detected. RanBPM, a scaffold protein that is known to interact with VASA protein (YDBIOI6681Puverel et al., 2011; Shibata et al., 2004), also exhibited the expression pattern similar to VASA in adult marmoset testis. The nucleocytoplasmic expression of marmoset RanBPM was observed in MARWI$^+$ spermatocytes and round spermatids but not in the elongating spermatids (Fig. 3D). On the other hand, a synaptonemal complex protein SYCP1 and a haploid germ cell-specific RING finger protein HAPRIN (YDBIOI6681Kitamura et al., 2005; Kitamura et al., 2003) displayed more restricted expression. Like cynomolgus monkeys and humans (YDBIOI6681Pousette et al., 1997; Yamauchi et al., 2009), marmoset SYCP1 was preferentially expressed in pachytene spermatocytes (Fig. 3E). HAPRIN was detected in the acrosomal region of spermatids following the initiation of spermiogenesis (Fig. 3F).

Meiosis-associated nuclear structures of marmoset germ cells during spermatogenesis

Meiotic male germ cells can be characterized by their unique chromosome structures, such as the XY body (de Vries et al., 2012) and synaptonemal complex assembly (Page and Hawley, 2004), at meiosis prophase I. The former is a chromatin domain composed of condensed sex chromosomes while the latter is involved in pairing homologous chromosomes. These structures can be marked by phosphorylated histone γH2AX and SYCP1 proteins respectively, and are organized predominantly in the pachytene spermatocytes of mice (YDBIOI6681Mahadevaiah et al., 2001; Monesi, 1965) and humans (YDBIOI6681de Vries et al., 2012; Pousette et al., 1997). Similarly, in marmoset testis, the dot-shaped single staining of γH2AX was detectable in the nuclei of DAZL$^+$VASA$^+$ pachytene spermatocytes while it was widely diffuse in the nuclei at earlier stages (Fig. 4A and B). The cells with a pronounced γH2AX focus also expressed SYCP1 protein (Fig. 4C and D). Thus, during marmoset spermatogenesis the nuclear localization of γH2AX and SYCP1 proteins clearly identified the formation of the XY body and synaptonemal complex in pachytene spermatocytes, but not in the early spermatocytes or the round spermatids.

Juvenile marmoset testis contains the unique germ cells expressing meiosis-associated genes

One of the unique features of primate reproduction is the existence of long pre-pubertal and pubertal periods before reaching sexual maturity (YDBIOI6681Chemes, 2001; Kelnar et al., 2002; Rey et al., 1993). At the juvenile phase in marmosets, we found a unique group of germ cells located in the luminal region of seminiferous tubules (Lin et al., 2012). Historically, these cells had been identified as 'pre-spermatogonia' that exhibit the morphological features corresponding to those of human gonocytes
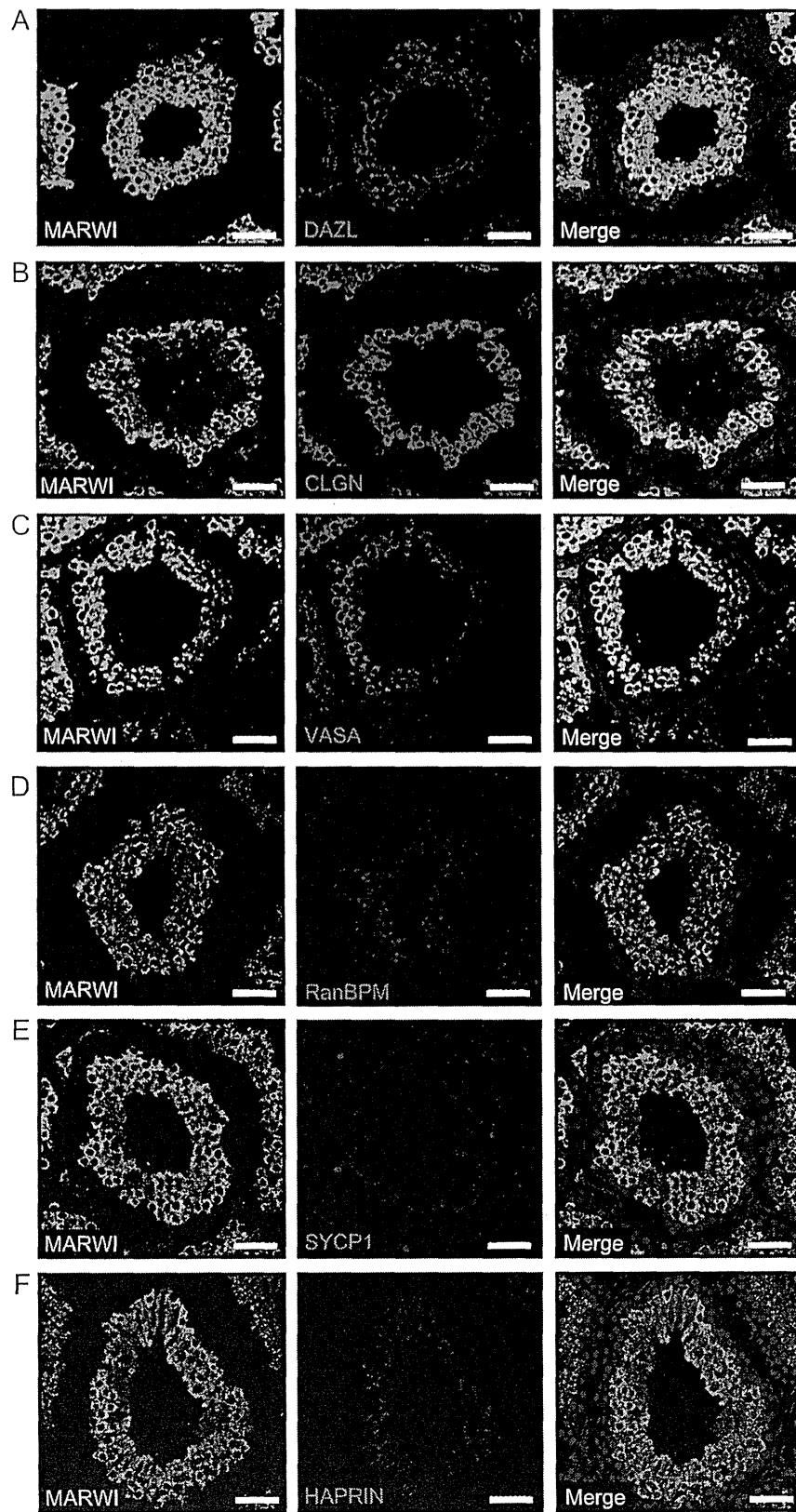
Fig. 3. Stage-specific expression of spermatogenesis-related proteins in adult marmoset testis. Confocal images of adult marmoset testis sections co-stained with antibodies against spermatogenesis-related proteins, including (A) anti-MARWI and anti-DAZL antibodies, (B) anti-MARWI and anti-CLGN antibodies, (C) anti-MARWI and anti-VASA antibodies, (D) anti-MARWI and anti-RanBPM antibodies, (E) anti-MARWI and anti-SYCP1 antibodies, and (F) anti-MARWI and anti-HAPRIN antibodies. Nuclei were counterstained with Hoechst 33342. Scale bar, 50 μm.